Particles II

Access the latest eBook →

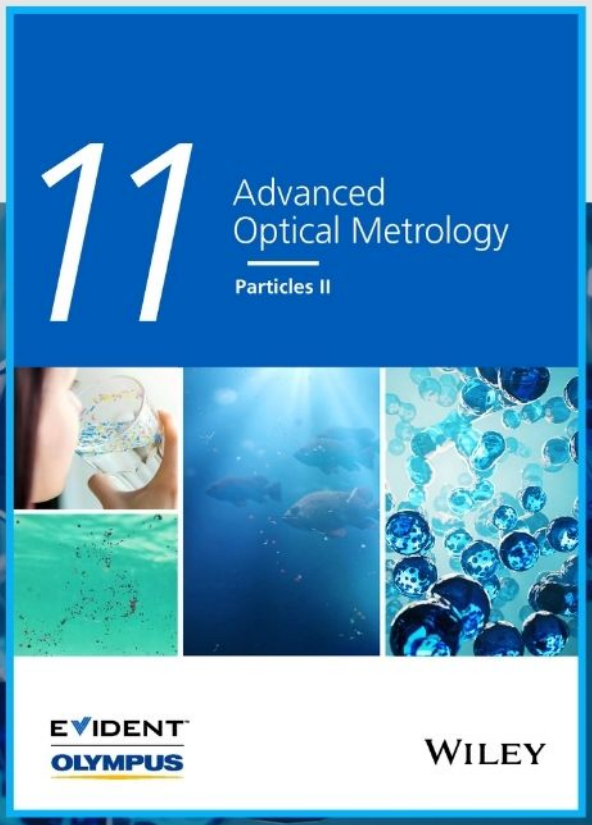

Impact on Biological Systems and the Environment

This eBook is dedicated to the research of Professor David Wertheim.
In collaboration with various groups, Professor Wertheim uses confocal microscopy to analyse the impact of different types of particles on human health and the environment, with a focus on human health-hazardous particles detected with solid-state nuclear track detectors (SSNTD). Download for free, today.

EVIDENT
OLYMPUS

WILEY

ADVANCED FUNCTIONAL MATERIALS
www.afm-journal.de

Band-Like Charge Transport in Phytic Acid-Doped Polyaniline Thin Films

Marco Ballabio, Tao Zhang, Chen Chen, Peng Zhang, Zhongquan Liao, Mike Hambsch, Stefan C. B. Mannsfeld, Ehrenfried Zschech, Henning Sirringhaus, Xinliang Feng,* Mischa Bonn,* Renhao Dong,* and Enrique Cánovas**

We explore the charge transport properties of phytic acid (PA) doped polyaniline thin films prepared by the surfactant monolayer-assisted interfacial synthesis (SMAIS). Structural and elemental analysis confirms the inclusion of PA in the thin films and reveals a progressive loss of crystallinity with the increase of PA doping content. Charge transport properties are interrogated by time-resolved terahertz (THz) spectroscopy. Notably, independently of doping content and hence crystallinity, the frequency-resolved complex conductivity spectra in the THz region can be properly described by the Drude model, demonstrating band-like charge transport in the samples and state-of-the-art charge carrier mobilities of ≈1 $cm^2V^{-1}s^{-1}$. A temperature-dependent analysis for the conductivity further supports band-like charge transport and suggest that charge carrier mobility is primarily limited by impurity scattering. This work highlights the potential of PA doped polyaniline for organic electronics.

1. Introduction

Conducting polymers are attractive electroactive materials for organic electronics since their conductivity can be tuned, reversibly, more than thirteen orders of magnitude under chemical doping and dedoping cycles.[1,2] The enhancement of the conductivity in these materials comes from the generation of extended states in doped molecules, that are generally attributed to the creation of quasiparticles (e.g., solitons and polarons), a view supported by optical spectroscopy and magnetic measurements.[3,4] The charge carrier transport in polymers is commonly described as a thermally activated process, a hopping mechanism associated with localized charge carriers. Thermally activated transport is enabled by charge carrier motion along the conjugated backbone (i.e., intra-chain, dominating at higher frequencies), and inter-chain processes between conductive domains dominating the long-range transport macroscopically (i.e., towards the DC limit). Within this picture, most work over the past decades has been devoted to engineering band-like charge transport in conducting polymers. To achieve that, both inter- and intra-molecular overlap

M. Ballabio, M. Bonn, E. Cánovas
Max Planck Institute for Polymer Research
55128 Mainz, Germany
E-mail: bonn@mpip-mainz.mpg.de; enrique.canovas@imdea.org
T. Zhang, P. Zhang, X. Feng, R. Dong
Center for Advancing Electronics Dresden (cfaed) and Faculty of Chemistry and Food Chemistry Chair of Molecular Functional Materials
Technische Universität Dresden Mommsenstraße 4
01069 Dresden, Germany
E-mail: xinliang.feng@tu-dresden.de; renhaodong@tu-dresden.de
T. Zhang
Key Laboratory of Marine Materials and Related Technologies
Zhejiang Key Laboratory of Marine Materials and Protective Technologies
Ningbo Institute of Materials Technology and Engineering
Chinese Academy of Sciences
Ningbo 315201, P. R. China
E-mail: tzhang@nimte.ac
T. Zhang
School of Chemical Sciences
University of Chinese Academy of Science
Beijing 100049, China
C. Chen, H. Sirringhaus
Optoelectronics Group
Cavendish Laboratory
JJ Thomson Avenue, Cambridge CB3 0HE, UK
Z. Liao, E. Zschech
Fraunhofer Institute for Ceramic Technologies and Systems (IKTS)
Maria-Reiche-Strasse 2, 01109 Dresden, Germany
M. Hambsch, S. C. B. Mannsfeld
Center for Advancing Electronics Dresden (cfaed) and Faculty of Electrical and Computer Engineering
Technische Universität Dresden
01062 Dresden, Germany
E. Cánovas
Instituto Madrileño de Estudios Avanzados en Nanociencia (IMDEA Nanociencia)
Madrid 28049, Spain

The ORCID identification number(s) for the author(s) of this article can be found under https://doi.org/10.1002/adfm.202105184.

DOI: 10.1002/adfm.202105184

of frontier orbitals is required to form a delocalized electronic band.[5,6] With this target in mind, many efforts have aimed at exploiting methods for improving the long-range ordering/crystallinity of conducting polymers, thereby hoping to maximize charge carrier delocalization within the polymer backbone.[7]–[10] Indeed, state-of-the-art results in terms of conductivity and mobility figures in conducting polymers are often linked with high crystalline samples. [11,12]

In this work, we prepare ordered thin films of quasi two-dimensional polyaniline (q2D-PANI) with phytic acid (PA) as a dopant during surfactant monolayer assisted interfacial synthesis (SMAIS).[12] This singular dopant does have six phosphate groups that could release more than one proton per molecule; furthermore, PA is expected to enable the coordination of multiple aniline sites, acting then as a bridge between adjacent conductive domains to improve long-range transport in the samples. [13]

Following SMAIS synthesis, we observed that PA concentrations as low as 3 mM in PANI produced an optical density at 800 nm, generally assigned to the polaron band, which is commensurate to the one obtained in q2D-PANI samples doped with up to 1 M HCl. Moreover, structural and compositional characterization for the PA doped PANI films (PA-PANI) revealed a reduced crystallinity when compared with HCl-doped PANI, [12] indicating that the PA dopant is perturbative towards crystal structure. Increasing the PA dopant concentration from 3 mM to 75 mM, the PANI film becomes increasingly amorphous. To study the impact of PA doping on the sample´s conductivity, we characterized the frequency-resolved complex conductivity in the THz region by time-resolved THz spectroscopy (TRTS). The results demonstrated that, remarkably, Drude-like band conduction in all samples independently of doping content, and then, independently of their degree of crystallinity. Even the most-doped, least-crystalline, analysed samples revealed the highest charge carrier scattering rates and corresponding the highest mobility (1 $cm^2V^{-1}s^{-1}$) and conductivity (ca. 93 S cm^{-1}). This counterintuitive result indicates that while PA seems to promote structural disorder, it does increase energetic order;, e.g., this could be eventually linked with PA promoting cross-linking between conductive domains in PA-PANI. Cross linking could be able to enable long-range charge transport even in poorly crystalline samples, a result that might align with the findings of previous reports where high mobility have been observed in highly disordered or even amorphous samples.[14] Finally, temperature-dependent experiments reveal a scattering rate barely affected by temperature, indicating that impurity scattering is the limiting mechanism in the mobility for the PA doped PANI samples.

2. Results and Discussion

The synthesis procedure for PA-PANI by SMAIS is similar to the one described previously and summarized in **Figure 1**.[12] In brief, a surfactant (sodium oleyl sulfate) monolayer was prepared on the water surface in a glass well (50 mL, Ø = 6 cm), followed by the addition of aniline monomers (11.5 µL in 1 mL water) in the water sub-phase. The glass well was then covered with a petri dish and kept under 1°C. After 24 h, hydrochloric acid (HCl, 0.02 M), phytic acid (PA), and ammonium persulfate (APS, 2.5 mg in 1 mL water) were successively injected into the water sub-phase to trigger the polymerization. After a certain polymerization time (12-48 h), a uniform and continuous polymer film with a dark green color appeared on the water surface. The PA concentration was tuned on different samples as 3 mM, 15 mM and 75 mM, yielding the PA-doped PANI film samples named hereof as PA3-PANI, PA15-PANI and PA75-PANI, respectively. As a contrast, we also synthesized HCl-doped PANI by the same protocol and controlled the doping content of HCl with 3 mM and 1 M, respectively.

The resultant PA-PANI film on water was robust enough to be transferred intact onto different substrates for morphological and structural characterizations. For instance, the PA-PANI film after 12 h polymerization could be suspended over large holes of ≈ 400 μm^2 on a TEM grid. (**Figure 2**a). Under the optical microscope, the PA3-PANI (prepared in 3 mM PA solution) transferred onto SiO_2/Si is homogenous, and the edges of the film are clearly visible (Figure 2b). Atomic force microscopy (AFM) measurement at film edges reveals an average thickness of 59±3 nm for 12-h reaction (Figure 2c). In the following studies, the reaction time for the preparation of the PA-PANI films was set as 12 h.

X-ray photoelectron spectroscopy (XPS) reveals that the PA3-PANI films contain carbon, nitrogen, phosphorus, chlorine, and oxygen in a ratio of 56.4%, 6.74%, 6.32%, 0.46%, and 30.09% (Figure 2d and Table S1), respectively. Two prominent peaks of N1s at 401.9 eV and 399.8 eV can be attributed to two types of nitrogen (-NH^+- and = NH-) in PA3-PANI (Figure 2e). The peak at 134.1 eV belongs to the -PO_4H_2 moiety of PA (Figure 2f). The three peaks of C1s signal can be assigned to C1s of C-C at 284.8 eV, C = C at 284.8 eV, C-N at 286.5 eV, and C-N at 288.2 eV (Figure S1), respectively. Fourier transform infrared spectroscopy of PA3-PANI shows the characteristic bands of quinoid and benzenoid rings at 1575 and 1498 cm^{-1} (Figure S2). Bands at 1302 and 1242 cm^{-1} arise from the C–N stretching of the secondary aromatic amine and C–N stretching vibration in the polaron structures, respectively. Meanwhile, the band at 1647 cm^{-1} is attributed to the stretching frequencies of the P = O groups. Confocal Raman characterization on the PA3-PANI film also supports the formation of PA-PANI (details shown in SI, Figure S3).

The UV-Vis spectra of PA3-PANI film reveals a similar absorbance with that of HCl-doped PANI (Figure S4).[1,15,16] The feature at 400 nm (≈3 eV) is generally assigned to the π-π^* transition of the benzenoid ring.[15] On the low energy side, the asymmetric absorption band peaking around 800 nm (≈1.5 eV) is attributed to the transition from the π level to a polaron state, which is generally considered for the fingerprint of the protonated, conductive emeraldine salt.[3,4,15] Note that the peak (around 800 nm) disappeared completely when the film was dedoped by 1 M NH_4OH (Figure S5). However, in comparison to the 1M HCl doped q2D-PANI, the polaron band of PA3-PANI seems to extend towards the IR, which can be an indicator of more delocalized conductive states.[16] Furthermore, it is remarkable how the absorption strength for the polaron band of just 3mM doped PANI is comparable with the one made by 1M HCl doping, a possible consequence of PA promoting a more efficient doping per molecule.

Figure 2g shows the representative selected area electron diffraction (SAED) patterns of PA3-PANI along the [001] axis, which reveals a hexagonal lattice with the $[\bar{1}010]$ and $[0\bar{1}10]$ reflections at 3.06 nm^{-1}, corresponding to in-plane spacing of $a = b = 0.38$ nm (Figure S6). This SAED patterns were reproducible at different positions in the PA3-PANI film (Figure S7).

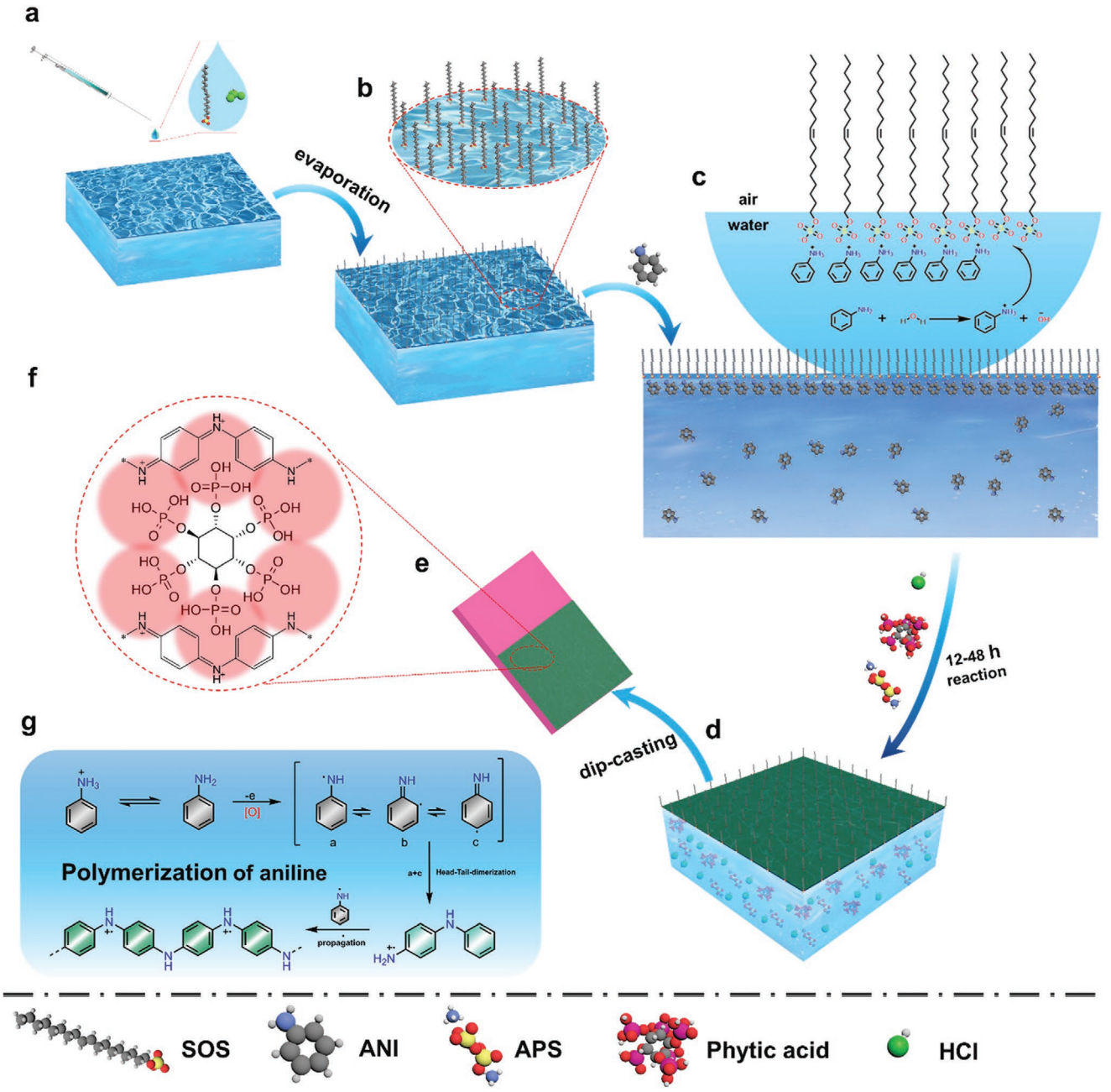

Figure 1. Schematic illustration of the synthesis procedure for PA-PANI. a) Addition of the surfactant (sodium oleyl sulfate, SOS) solution on water surface. b) Formation of surfactant monolayer after the evaporation of solvent. c) Addition of the aniline (ANI) monomer into the water sub-phase, in which aniline monomers can adsorb onto the surfactant monolayer due to electrostatic interactions and hydrogen boning. d) Oxidative polymerization triggered by ammonium persulfate (APS), phytic acid (PA), and HCl. e) Transfer of the film onto the substrate. f) Scheme of the proposed arrangement between phytic acid and the polyaniline chains. g) Polymerization reaction mechanism of aniline monomers.

Grazing-incidence wide-angle X-ray scattering (GIWAXS) shows that the PA3-PANI film is polycrystalline at a microscopic scale with out-of-plane c = 1.31 nm (Figure 2h-i). As such, the molecular structure of the PA3-PANI can be proposed as shown in Figure 1f, where the adjacent PANI chains along the in-plane direction are bridged by the phosphate groups of the PA dopant. Note that the same SMAIS protocol employed for developing HCl doped PANI samples led to highly ordered, quasi two-dimensional samples with square symmetry.[12] That is, despite following almost the same synthetic approach, the addition of PA in PANI samples was perturbative upon the crystallinity of the final film.

After the preliminary characterization that confirms the inclusion of PA acid molecules in the ordered structure of PA3-PANI, we characterized the effect of doping content on the samples. Figure 3a shows the absorbance spectra of PA-PANI thin films samples doped with 3, 15, and 75mM of PA. The amplitude of the absorption band peaking around 800nm increases significantly with the increase of added concentrations of PA. XPS spectra in **Figure 3**b show that the element ratios of P:N in the

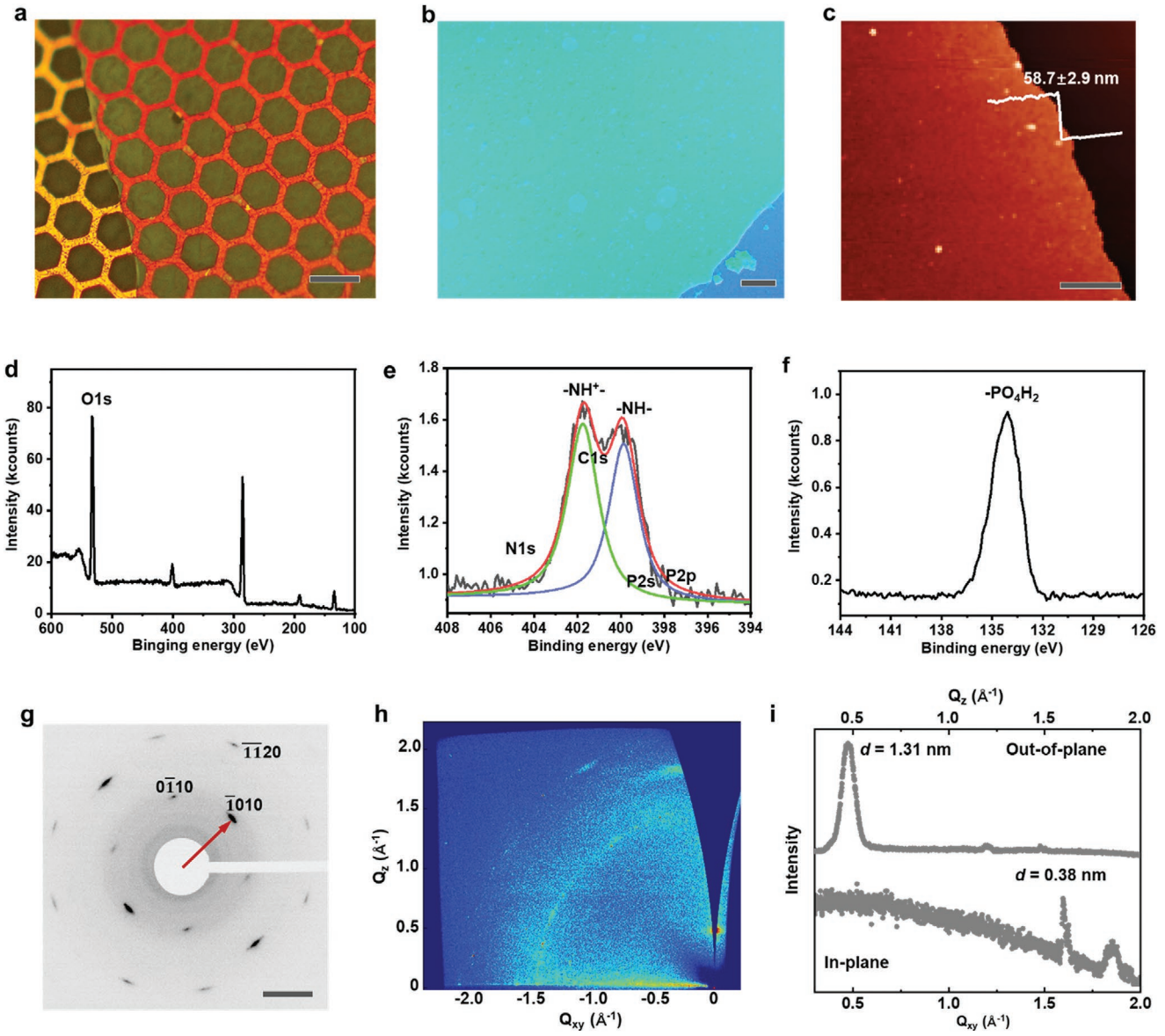

Figure 2. Characterization of PA3-PANI films. Optical microscopy images of PA3-PANI film a) suspended over a copper grid and b) transferred onto SiO_2/Si wafer. c) Atomic force microscopy (AFM) image and thickness value of PA3-PANI after the 12-h reaction. d) XPS spectrum and e) high-resolution N1s and f) P2p core level spectrum of PA3-PANI. The fitting in (e) was performed with a set of Voigt peaks. g) SAED pattern of PA3-PANI along the [0001] axis, the $[\bar{1}010]$ and $[0\bar{1}10]$ reflections are at 3.06 nm^{-1}. h) GIWAXS pattern of PA3-PANI on a Si wafer. i) In-plane and out-of-plane projections from (g). Scale bars: (a-b) 20 µm; (c) 2 µm; (g) 2 nm^{-1}.

resultant PA-PANI films are 0.46 (3 mM), 0.64 (15 mM), and 0.94 (75 mM), respectively. In addition, high-resolution N1s core level spectra show that the contents of doped/charged N in PA-PANI films are 53.80%, 59.48%, and 83.44%, respectively, which are an estimate for the doping level of the samples (Figure 3c). These results demonstrate that the doping level of PA-PANI can be controlled by increasing PA concentrations during the SMAIS synthesis. The dedoped sample (by 1 M NH_4OH) was characterized by an absorption band centered at ≈650 nm (≈1.9 eV, Figure S5), which can be attributed to the HOMO-LUMO transition of the emeraldine base, a non-conductive form of polyaniline.[17] Furthermore, GIWAXS results show that the increase of PA content leads to a decrease in structural order in the PA doped PANI films (Figure 3d), which we attribute to a large steric effect of PA molecules as well as the strong interaction between PA and PANI chains.

TRTS is an all-optical, contact-free method capable of addressing the nature of charge transport in a given sample by providing the complex photoconductivity in the THz frequency region. In a conventional measurement, we photo-excite the sample with a 50 fs laser pulse centered at 800 nm. After the absorption of the pump beam, a THz probe pulse interrogates the photoconductivity of the sample in a non-invasive way. The THz pulse is generated by the same laser system via optical rectification in a ZnTe crystal providing a bandwidth of 0.3-2.5 THz[18]– .[20] By definition, we can express the photoconductivity in the sample as $\Delta\sigma = -e\,\Delta N\,\mu$, where e is the electron charge, ΔN the variation in charge carrier density induced by the pump, and μ is the

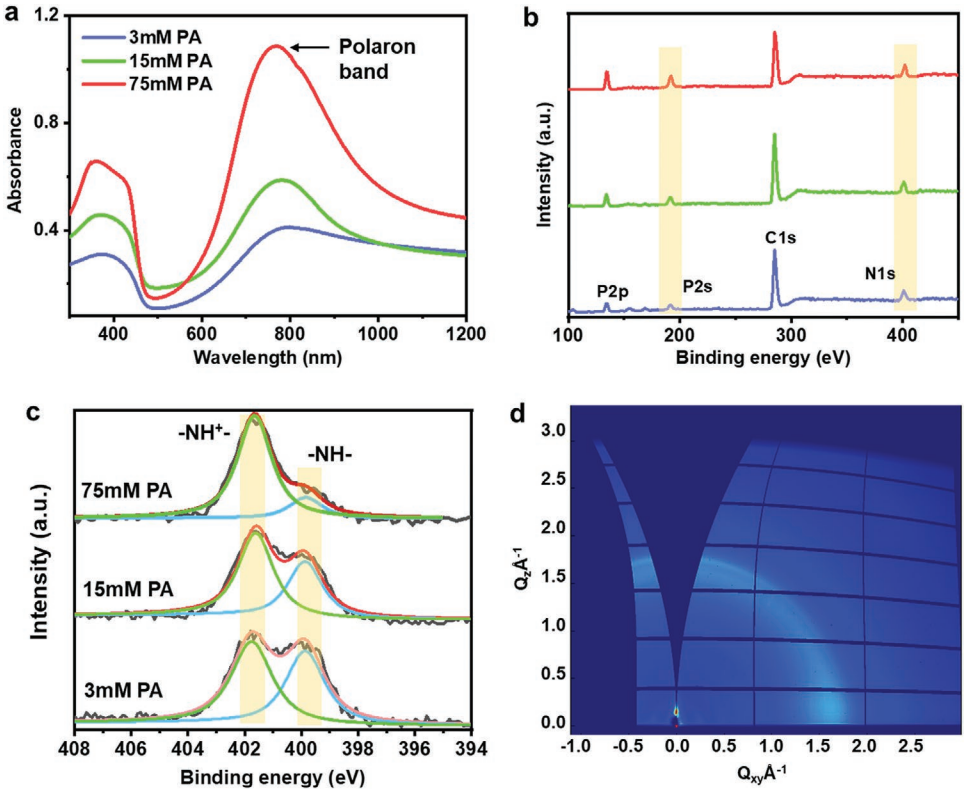

Figure 3. Characterizations of PA-PANI films with different PA contents. a) UV-Vis-NIR absorption spectra of PA-PANI prepared with 3 mM (blue), 15 mM (green) and 75 mM (red) PA, respectively. b) XPS survey spectra of the samples in (a), from which the element ratio of P:N in PA-PANI films can be calculated: 0.46 (3 mM), 0.64 (15 mM), and 0.94 (75 mM), respectively. c) High-resolution N1s core level spectra of the PA-PANIs in (a), from which the ratios of doped/charged N in PA-PANI can be calculated: 53.80% (3 mM), 59.48% (15 mM), and 83.44% (75 mM), respectively. d) The typical GIWAXS pattern of the 75PA-PANI film.

sample's mobility. Following an optical pump-THz probe scheme (OPTP), we can obtain sub-ps dynamics linked with photoinduced changes for the real and imaginary components of the conductivity. In **Figure 4**a, we plot the real part of conductivity as a function of pump-probe delay for the set of PA doped samples shown in Figure 3 (all samples are ≈100nm in thickness, photon excitation intensity of $4.4 \cdot 10^{19}$ photons/m^2 at 1.55eV). Under the employed experimental conditions, we find that all PA doped samples are characterized by an abrupt rise in photoconductivity induced by the pump, which is followed by a decay that can be phenomenologically modeled with a double exponential function. The best fit to the data returns lifetime values of $t_1 = 0.8 \pm 0.1$ ps and $t_2 = 52 \pm 2$ ps for the fast and slow components, respectively. The obtained dynamics resemble those reported

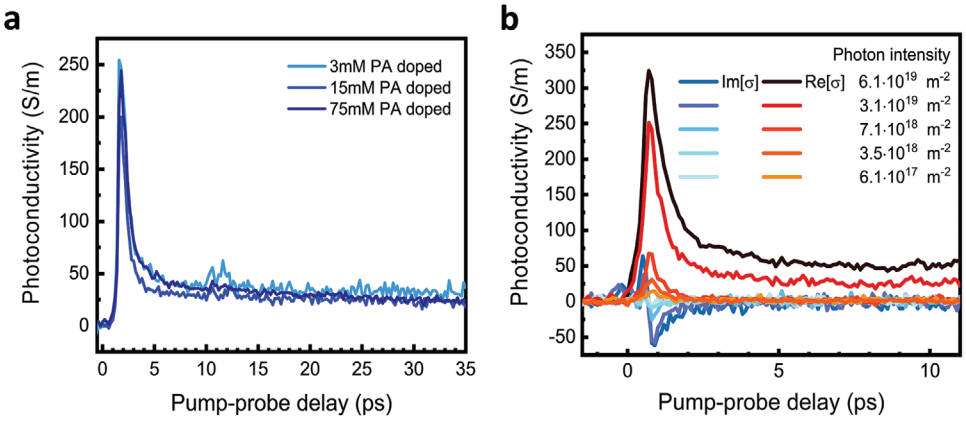

Figure 4. a) Photoconductivity from optical pump-THz probe on 3, 15 and 75 mM PA doped PANI sample (blue lines) under a photon intensity of $4.4 \cdot 10^{19}$ m^{-2}. b) Real (positive red traces) and imaginary (negative blue traces) parts of the time-resolved photoconductivity in 75 mM doped PANI as a function of excitation density.

previously in THz studies in other conventional organic semiconducting polymers,[21,22] where the fast initial decay is generally assigned to charge trapping and/or to the condensation of quasi-free charges that thermalize into bound, neutral excitons. In both scenarios, the fast decay represents pump-induced species that do not contribute to the photoconductivity beyond 1ps. On the other hand, the long-lived 50 ps component strongly suggests that a significant fraction of photo-induced species are conductive, that is, they are not falling immediately into bound states. Note that this holds independently of sample crystallinity.

To further understand the nature of the observed charge dynamics and investigate whether excitons are present in the samples beyond 1ps, we analyze the dependence of the photoconductivity as a function of impinging photon flux for the 75 mM doped PANI sample (the analysis for the low-doped samples can be found in Figure S9-10). Figure 4b presents a summary of the OPTP data obtained as a function of photon intensity (in the range between $\approx 6 \cdot 10^{17}$ and $\approx 6 \cdot 10^{19}$ photons/m^2). The negative signals represent the dynamics for the imaginary component of the pump-induced conductivity, monitored by following pump-induced phase shifts in the THz waveform as a function of time. Changes in the phase of the propagating THz probe are linked to the imaginary conductivity component and are indicative of polarizable neutrally charged excitons in the samples. As evident from Figure 4b, imaginary dynamics are defined by only an ultrafast decay that completely vanishes within 2 ps, independently of adopted fluence. This behaviour is consistent with a lack of polarizable excitons in the samples. The observed timescale of the imaginary conductivity deactivation matches fairly well the short lived component resolved for the real conductivity in the samples as a function of time and can be tentatively interpreted in terms of free photoexcited species that undergo ultrafast charge trapping.[23] On the other hand, the long-lived real conductivity should be attributed to a residual population of delocalized free charge carriers in the sample. Fluence dependence analysis for the real conductivity component in Figure 4b also shows an onset for the appearance of the long-lived component above an excitation density of $\approx 10^{19}$ photons/m^2, which can give an indication about the number of active traps in the material, that is, the emergence of the signal could be linked with trap filling effects.

The previous analysis on carrier dynamics inferred from TRTS strongly indicates that free delocalized charge carriers are the main products in the samples for excitations above $\approx 10^{19}$ m^{-2} and timescales above ≈2ps. We can corroborate whether these findings are correct by addressing the nature of charge transport in the samples, this can be accomplished by analysing the frequency-resolved complex conductivity of the signals in our THz spectral window (between 0.3 and 2.3 THz, limited by the output of our ZnTe emitter). In **Figure 5** we present the conductivity spectra of all PA-PANI samples analyzed in this work, obtained by the Fourier transform of the time domain transmitted pulses. In these experiments, the excitation fluence equals $4.4 \cdot 10^{19}$ m^{-2}; conductivity traces were collected 10 ps after the photoexcitation. Independently of the doping content, we resolved a decreasing real and increasing imaginary conductivity component with frequency within the probed THz region. Remarkably, all traces can be described fairly well by the Drude model:[24]

$$\sigma_{Drude} = \frac{\varepsilon_0 \omega_p^2 \tau}{1 - i\omega\tau} \quad with \quad \omega_p^2 = \frac{Ne^2}{\varepsilon_0 m^*} \tag{1}$$

Where ω_p is the plasma frequency, N is the charge density, e the elementary charge, m^* is the effective mass for the monitored charge carriers, ε_0 is the vacuum permittivity, and τ is the mean averaged scattering time. The Drude model is sufficient for all doping concentrations to explain the data. As such, we can conclude that the long-lived signals in OPTP dynamics refer unambiguously to free, delocalized charge carriers populating PA-doped PANI samples. It is worth mentioning here that Lee et al. have previously reported band-like Drude-like behavior in highly crystalline PANI samples doped with camphor sulphonic acid. [11] In that case, they derived the real conductivity from Kramers-Kronig analysis on reflectivity spectra, in a frequency range limited above 500 cm^{-1} (>15 THz). The traces shown in Figure 5 reveal Drude responses from fits to the complex-valued conductivity and for frequencies as low as ≈10 cm^{-1} (0.3 THz). This allows us to fully rule out an eventual drop for the conductivity towards the DC limit, an aspect that is generally a fingerprint for charge carrier localization.[25]

From the best fit of our data to Eq.1, we can estimate a scattering time $\tau < 10$ fs for the samples doped by 3 and 15 mM PA,

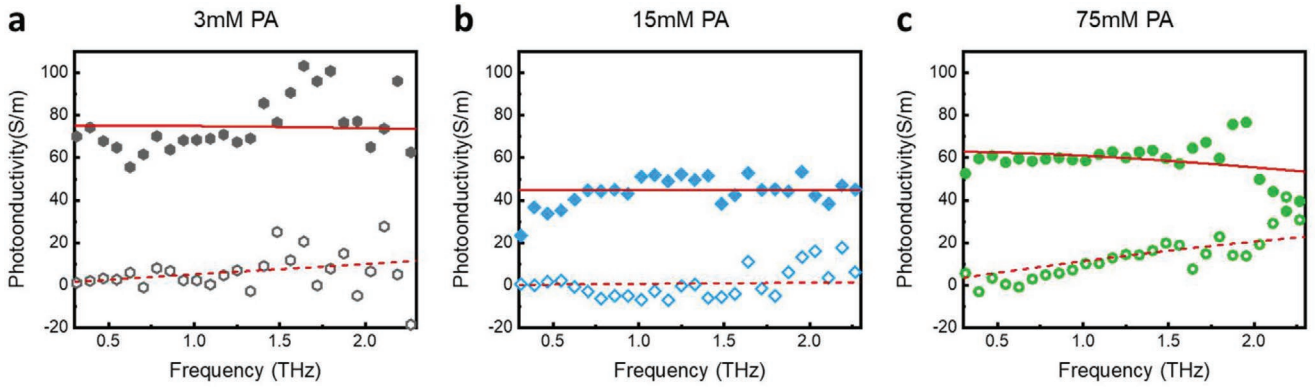

Figure 5. Frequency resolved photoconductivity of PA-PANI doped by a) 3 mM, b) 15 mM and c) 75 mM of phytic acid, measured 10ps after photoexcitation. Full and empty symbols denote the real and the imaginary parts of the complex photoconductivity, respectively. Red solid and dashed lines represent the best fit to the data, according to the Drude model.

and a τ of 29 ± 3 fs for the 75 mM PA doped sample. This observation reveals that the mobility of the samples is affected by doping content within the analyzed range. That is, doping affects not only the charge carrier density available for conduction but also their mobility. In previous reports scattering rates of 22–27 fs were reported in state-of-the-art PANI samples doped by camphor sulphonic acid.[11,26] Interestingly, we obtain the longer carrier scattering time for the sample that presents the lowest degree of crystallinity. While these observations may seem counterintuitive, they can be rationalized by taking into account that structural order and energetic order are not necessarily unequivocally correlated. Note that state-of-the-art mobilities up to ≈1 $cm^2\ V^{-1}\ s^{-1}$ have been recently reported also in materials displaying low crystallinity or even, in some cases, of amorphous nature; for example, within these reports, high mobilities have been attributed to a network of tie chains providing interconnecting transport pathways between conducting domains.[6,14,27] This crosslinking effect might be suppressed in highly ordered structures (see Figure S12). Furthermore, if a specific dopant is perturbative towards morphology (e.g., improves polymer chain planarity), it might have a beneficial role towards intra-chain conductivity, provided that torsional effects along the backbone are well known to produce localized states.[28,29] It is worth to note that the PANI doped by 75 mM PA (i.e., 75PA-PANI) gives an electric conductivity of ≈93 S cm^{-1} (Figure S18), which is superior to the highly crystalline PANI doped by 1 M HCl with 23 S cm^{-1}, further demonstrating the powerful doping effect of PA.[30]

The scattering time, together with the effective mass, is the quantity that determines the electrical mobility following the relation $\mu = \frac{e\tau}{m^*}$. According to most of the literature, there are two scenarios that have been linked with Drude-like responses in PANI samples, the presence of free band-like charge carriers or polarons,[11,31,32] the main difference regarding mobility estimates between both scenarios resides on the assumed effective mass for the populating charge carriers. Note that their spectral response in the THz region is not easily distinguishable.[33] If we assume that polarons (rather than free electrons) are the conductive species that are linked to the monitored Drude responses, we can estimate the mobility of PA75-PANI as 0.91 ± 0.09 $cm^2V^{-1}s^{-1}$ (or, 30 ± 3 $cm^2V^{-1}s$), where an effective mass of $M_{pol} = 56m_e$ is considered for polarons,[31] (alternatively, $m^* \approx 1.7m_e$ for free electrons).[11]

To better understand the nature of the transport in the PA-PANI samples, we performed a temperature-dependent TRTS analysis. **Figure 6**a, shows the impact of temperature on the time-resolved real part of the conductivity. The data reveal an increase in the monitored photoconductivity as the sample temperature is reduced from 300K to 77K (Figure 6a). This is an exceptional behavior for conductive polymers that usually exhibit thermally activated transport.[34] In Figure 6b, we present the frequency-resolved conductivity for the upper and lower limit tested temperatures for a 75mM doped PA-PANI sample (rest of the data can be found in Figure S13-14). For cooling the sample, it must be contained in a cryostat under vacuum. Under vacuum, the Drude response seems to be modified to a Drude-Smith (DS) response, [19] possibly from the degassing of the sample. The DS model accounts for Drude-like free carriers which experience some degree of preferential backscattering (see SI for further details). In any case, the data in Figure 6b reveals that the conductivity of the sample improves with decreasing temperature, also in the DC limit (when $\omega \to 0$). The frequency-resolved complex conductivity spectra collected at every temperature show a clear free-carrier response. From fits to the DS model (solid and dashed lines in Figure 6b), we can obtain the variation of scattering rate and plasma frequency as a function of temperature and then scrutinize the origin for the unexpected increase in conductivity at reduced temperatures. Figure 6c summarizes the parameters obtained from the DS fits for two different samples of PA-PANI doped with 75 mM. The data reveals that the scattering rate is barely dependent on temperature, an observation that is in line with previous reports on band-like transport in PANI (see Figure S16) and suggests impurity scattering as a limiting factor for the charge carrier mobility.[35] Furthermore, the plasma frequency increases by approximately a factor of 2 from 290 to 77K. The increase in plasma frequency seems to explain alone the observed increase in conductivity at lower temperatures. An increase in plasma frequency $\left(\omega_p = \sqrt{\frac{Ne^2}{m^*\varepsilon_0}}\right)$ could be rationalized with either an increase in photo-induced carrier density (N, where $N = \xi \cdot A \cdot N_{hv}$, where A refers to the fraction of absorbed photons and ξ is the photon to free carrier yield) and/or a reduction in free carrier effective mass. Provided that the amount of absorbed photons N_{hv} does not change with temperature (see Figure S11, S17), we speculate that an

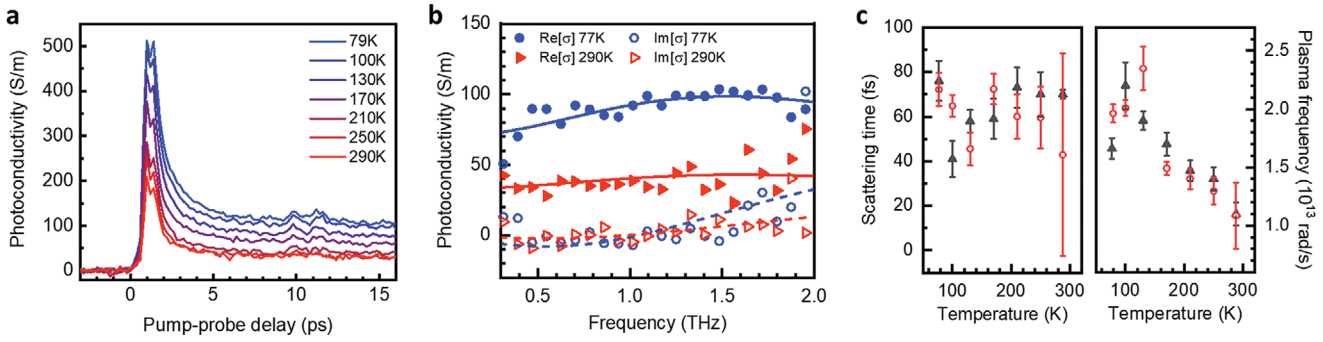

Figure 6. a) Time-resolved photoconductivity as a function of temperature b) Complex-valued photoconductivity spectra at 77K (blue circles) and 290K (red triangles); solid lines are the real and imaginary components from Drude-smith fits. c) Scattering times (left) and plasma frequencies (right) obtained from Drude-Smith analysis as a function of temperature for 2 sets of samples.

enhanced yield could be related with trap filling effects induced by a T-dependence of the background doping. Alternatively, a decrease in effective mass by reducing T has been suggested theoretically as a fingerprint of weak e-ph coupling in rubrene crystals displaying band-like transport signatures.[36,37] At this stage we are unable to conclude the dominant mechanism, in any case, these observables do not alter the main conclusion derived from the T dependent analysis: impurity scattering limits free charge carrier motion in the samples. An observable which seems reasonable taking into account the non-crystalline nature of the analysed samples.

3. Conclusion

In conclusion, we investigated the charge transport properties of polyaniline thin films achieved by SMAIS doped with a novel phytic acid dopant. Structural and elemental analysis confirms the inclusion of PA in the thin films and confirms a progressive loss of structural order as the PA doping content is increased. Independently of doping content, the frequency-resolved complex conductivity spectra can be explained by the Drude model, revealing band-like transport in the samples. We found enhanced charge carrier mobilities for higher doping, despite the samples being notably less crystalline. This anti-correlation between conductivity and the degree of order in the samples indicates that while PA seems to promote structural disorder, it does increase energetic order (e.g., by enabling long-range charge transport between adjacent conductive domains). Finally, the temperature-dependent conductivity does not show any sign of thermally activated charge transport, in line with the notion of band-like conduction and loosely bound charge carriers.

4. Experimental Section

Material: Aniline, sodium oleyl sulfate (SOS), phytic acid aqueous solution (w/w:50%), Ammonium hydroxide solution (w/w:28%) and hydrochloric acid (37%) were obtained from Sigma-Aldrich. Ammonium persulfate and chloroform were purchased from Alfa Aesar. Aniline was purified by reduced pressure distillation before using, and the other chemicals were used as received.

Synthesis of PA-PANI: The synthesis procedure is similar to our previous reports.[12] The surfactant solution was obtained by dissolving SOS in chloroform (1 mg mL^{-1}) and filtered by PFTE syringe filter (0.2 µm, 1–15 mL, ThermoFisher). 50 mL Millipore water in a crystalline dish (Ø = 60 mm) was placed in a refrigerator (Liebherr FKUv 1660 Premium, Germany) at 1°C for 40 min. Then, 10 µL of the surfactant solution was spread onto the surface of the water. After the complete evaporation of chloroform, which lasts 30 minutes, 1 mL of aniline aqueous solution (11.5 µL mL^{-1}, 0.13 mol L^{-1}) was gently injected into the water subphase with a pipette. After 24h to allow for the diffusion and adsorption of monomers onto the air-water interface, a certain amount of phytic acid aqueous solution (e.g., 0.160–3.87 mL, w/w:50%) and 1 mL ammonium persulfate solution (10 mg mL^{-1}, 0.044 mol L^{-1}) were added into the subphase in 30 min, respectively. Finally, the reaction dish was covered by a glass slide in the refrigerator for oxidative polymerization. The solution turned gradually from dark blue to dark green in 48 hours, indicating a successful polymerization of aniline monomers into PANI. A shining and continuous film appears on the surface of water, which can be transferred onto arbitrary substrates. To remove unreacted monomers and excess phytic acid, the q2D PANI-PA film on substrate was rinsed for ≈1 h with chloroform (20 mL) and ethanol (20 mL), respectively.

Dedoping of PA-PANI: The q2D PANI-PA was dedoped in alkaline solution, which was prepared by dissolving 3 mL ammonium hydroxide solution (w/w:28%) in 40 mL ethanol-water solution (volume ratio, ethanol: water = 2:1). The synthesized PANI film was transferred onto surface of the alkaline solution with a coverslip, and the film turned from dark green to dark blue, indicating a completion of PANI dedoping.

Time-resolved THz Spectroscopy: The measurements were performed using a standard optical pump-THz probe setup driven by a titanium: sapphire laser amplifier system generating ≈100 fs width laser pulses with a central wavelength of 800 nm, and a repetition rate of 1 kHz. The laser output is used for the optical pump and for the THz generation by optical rectification on a 1mm slab of ZnTe cut along the (110) plane. This ensures a THz spectrum between 0.3 and 2.5 THz. The detection of THz pulses is performed via electro-optical sampling on an identical ZnTe crystal.

Other characterizations: The morphology and structure of the PA-PANI films were investigated by transmission electron microscopy (Zeiss, Libra 200 kV) and optical microscopy (Zeiss) with a Hitachi KP-D50 color digital CCD camera. GIWAXS measurements were carried out at the KMC-2 beamline at Helmholtz-Zentrum Berlin. The beam energy was 12.4 keV (λ = 1 Å) and the detector-to-sample distance (342.2 mm) was verified using a LaB6 calibration standard. The beam incidence angle was 0.12° and the sample was exposed for 600 s to the beam. XPS measurements were performed on a PHI-5000C ESCA system with a monochromatic Mg Kα X-ray source (hv = 1253.6 eV), the C 1s value was set at 284.6 eV for charge corrections. Raman spectra were measured on a NT-MDT confocal spectrometer with a 532 nm laser, and the spot size of the laser beam was ≈0.5 µm. Infrared spectra were recorded on a FT-IR Spectrometer Tensor II (Bruker) with an ATR unit. UV-Vis absorption spectra were obtained on an UV-Vis-NIR Spectrophotometer Cary 5000 at room temperature. Atomic force microscopy (AFM) images were recorded in air on a customized Ntegra Aura/Spectra from NT-MDT (Moscow, Russia) with a SMENA head in semi-contact mode. The probes have a typical curvature radius of 6 nm, a resonant frequency of 47–50 kHz, and a force constant of 0.35–6.10 N m^{-1}. Height determination and calculation was performed with the software Nova Px 3.2.5 from NT-MDT and the free software Gwyddion.

Supporting Information

Supporting Information is available from the Wiley Online Library or from the author.

Acknowledgements

M.B and T.Z. contributed equally to this work. E.C. acknowledges financial support from the Max Planck Society, the regional government of Comunidad de Madrid (2017-T1/AMB-5207 & P2018/NMT-4511) and the "Severo Ochoa" Programme for Centres of Excellence in R&D (MINECO, Grant No. SEV-2016-0686). R.D. and X.F. acknowledge the funding support from EU Graphene Flagship (GrapheneCore3, No. 881603), ERC starting grant (FC2DMOF, No. 852909), ERC Consolidator Grant (T2DCP), and CRC 1415 (Chemistry of Synthetic Two-Dimensional Materials, No. 417590517). RD, X.F., M.H. and S.C.B.M. would also like to acknowledge the German Science Council, Centre of Advancing Electronics Dresden, EXC1056 (Center for Advancing Electronics Dresden). T.Z. acknowledges the National Natural Science Foundation of China (Grant No. 52003279) and Excellent Youth Foundation of Zhejiang Province of China (Grant No. LR21E030001). We thank HZB for the allocation of synchrotron radiation beamtime and Daniel Többens for help with setting up the measurements.

Open access funding enabled and organized by Projekt DEAL.

Conflict of Interest

The authors declare no conflict of interest.

Data Availability Statement

The data that support the findings of this study are available from the corresponding author upon reasonable request.

Keywords

band-like charge transport, conducting polymers, interfacial synthesis, polyaniline, thin films

Received: May 31, 2021
Revised: July 15, 2021
Published online: August 6, 2021

[1] M. Wan, J. Yang, *J. Appl. Polym. Sci.* **1995**, *55*, 399.
[2] E. S. Matveeva, *Synth. Met.* **1996**, *83*, 89.
[3] G. Zotti, G. Schiavon, *Synth. Met.* **1989**, *30*, 151.
[4] A. J. Epstein, J. M. Ginder, F. Zuo, R. W. Bigelow, H. S. Woo, D. B. Tanner, A. F. Richter, W. S. Huang, A. G. MacDiarmid, *Synth. Met.* **1987**, *18*, 303.
[5] Z. H. Wang, E. M. Scherr, A. G. MacDiarmid, A. J. Epstein, *Phys. Rev. B* **1992**, *45*, 4190.
[6] R. Noriega, J. Rivnay, K. Vandewal, F. P. V. Koch, N. Stingelin, P. Smith, M. F. Toney, A. Salleo, *Nat. Mater.* **2013**, *12*, 1038.
[7] K. Kang, S. Watanabe, K. Broch, A. Sepe, A. Brown, I. Nasrallah, M. Nikolka, Z. Fei, M. Heeney, D. Matsumoto, K. Marumoto, H. Tanaka, S. I. Kuroda, H. Sirringhaus, *Nat. Mater.* **2016**, *15*, 896.
[8] I. Y. Choi, J. Lee, H. Ahn, J. Lee, H. C. Choi, M. J. Park, *Angew. Chemie – Int. Ed.* **2015**, *54*, 10497.
[9] H. Terrones, M. Terrones, E. Hernández, N. Grobert, J. C. Charlier, P. M. Ajayan, *Phys. Rev. Lett.* **2000**, *84*, 1716.
[10] R. A. Street, *Nat. Mater.* **2006**, *5*, 171.
[11] K. Lee, S. Cho, H. P. Sung, A. J. Heeger, C. W. Lee, S. H. Lee, *Nature* **2006**, *441*, 65.
[12] T. Zhang, H. Qi, Z. Liao, Y. D. Horev, L. A. Panes-Ruiz, P. S. Petkov, Z. Zhang, R. Shivhare, P. Zhang, K. Liu, V. Bezugly, S. Liu, Z. Zheng, S. Mannsfeld, T. Heine, G. Cuniberti, H. Haick, E. Zschech, U. Kaiser, R. Dong, X. Feng, *Nat. Commun.* **2019**, *10*, 4225.
[13] L. Pan, G. Yu, D. Zhai, H. R. Lee, W. Zhao, N. Liu, H. Wang, B. C. K. Tee, Y. Shi, Y. Cui, Z. Bao, *Proc. Natl. Acad. Sci. USA* **2012**, *109*, 9287.
[14] D. Venkateshvaran, M. Nikolka, A. Sadhanala, V. Lemaur, M. Zelazny, M. Kepa, M. Hurhangee, A. J. Kronemeijer, V. Pecunia, I. Nasrallah, I. Romanov, K. Broch, I. McCulloch, D. Emin, Y. Olivier, J. Cornil, D. Beljonne, H. Sirringhaus, *Nature* **2014**, *515*, 384.
[15] W. S. Huang, A. G. MacDiarmid, *Polymer (Guildf)* **1993**, *34*, 1833.
[16] A. G. MacDiarmid, A. J. Epstein, *Synth. Met.* **1994**, *65*, 103.
[17] R. P. McCall, J. M. Ginder, J. M. Leng, H. J. Ye, S. K. Manohar, J. G. Masters, G. E. Asturias, A. G. MacDiarmid, A. J. Epstein, *Phys. Rev. B* **1990**, *41*, 5202.
[18] C. Schmuttenmaer, *Chem. Rev.* **2004**, *104*, 1759.
[19] R. Ulbricht, E. Hendry, J. Shan, T. F. Heinz, M. Bonn, *Rev. Mod. Phys.* **2011**, *83*, 543.
[20] M. C. Beard, G. M. Turner, C. A. Schmuttenmaer, *Spectroscopy* **2002**, 910.
[21] E. Hendry, M. Koeberg, J. M. Schins, L. D. A. Siebbeles, M. Bonn, *Chem. Phys. Lett.* **2006**, *432*, 441.
[22] Z. Jin, D. Gehrig, C. Dyer-Smith, E. J. Heilweil, F. Laquai, M. Bonn, D. Turchinovich, *J. Phys. Chem. Lett.* **2014**, *5*, 3662.
[23] F. A. Hegmann, R. R. Tykwinski, K. P. H. Lui, J. E. Bullock, J. E. Anthony, *Phys. Rev. Lett.* **2002**, *89*, 227403.
[24] P. Drude, *Ann. Phys.* **1900**, *306*, 566.
[25] T. L. Cocker, D. Baillie, M. Buruma, L. V. Titova, R. D. Sydora, F. Marsiglio, F. A. Hegmann, *Phys. Rev. B* **2017**, *96*, 205439.
[26] T. Unuma, N. Yamada, A. Nakamura, H. Kishida, S. C. Lee, E. Y. Hong, S. H. Lee, O. P. Kwon, *Appl. Phys. Lett.* **2013**, *103*, 053303.
[27] G. Kim, S. J. Kang, G. K. Dutta, Y. K. Han, T. J. Shin, Y. Y. Noh, C. Yang, *J. Am. Chem. Soc.* **2014**, *136*, 9477.
[28] J. M. Ginder, A. J. Epstein, A. G. MacDiarmid, *Solid State Commun.* **1989**, *72*, 987.
[29] J. M. Ginder, A. J. Epstein, A. G. Macdiarmid, *Synth. Met.* **1991**, *43*, 3431.
[30] T. Zhang, H. Qi, Z. Liao, Y. D. Horev, L. A. Panes-Ruiz, P. S. Petkov, Z. Zhang, R. Shivhare, P. Zhang, K. Liu, V. Bezugly, S. Liu, Z. Zheng, S. Mannsfeld, T. Heine, G. Cuniberti, H. Haick, E. Zschech, U. Kaiser, R. Dong, X. Feng, *Nat. Commun.* **2019**, *10*, 4225.
[31] R. P. McCall, J. M. Ginder, M. G. Roe, G. E. Asturias, E. M. Scherr, A. G. MacDiarmid, A. J. Epstein, *Phys. Rev. B* **1989**, *39*, 10174.
[32] R. Patil, Y. Harima, K. Yamashita, K. Komaguchi, Y. Itagaki, M. Shiotani, *J. Electroanal. Chem.* **2002**, *518*, 13.
[33] D. Emin, *Phys. Rev. B* **1993**, *48*, 13691.
[34] V. Coropceanu, J. Cornil, D. A. da Silva Filho, Y. Olivier, R. Silbey, J. L. Brédas, *Chem. Rev.* **2007**, *107*, 926.
[35] D. Chattopadhyay, H. J. Queisser, *Rev. Mod. Phys.* **1981**, *53*, 745.
[36] Y. Li, Y. Yi, V. Coropceanu, J. L. Brédas, *Phys. Rev. B – Condens. Matter Mater. Phys.* **2014**, *90*, 245112.
[37] X. Wang, A. Dodabalapur, *Appl. Phys. Lett.* **2020**, *116*, 093301.